SUPPORTING INFORMATION

Unprecedented ferrocene-quinoline conjugate: facile proton conduction *via* 1D helical water chains and selective chemosensor for Zn(II) ion in water

*Joseph Ponniah S[a], Subrat Kumar Barik[a], Rosmita Borthakur[a], Arunabha Thakur[a], Bikash Garai[b], Sourita Jana[a] and Sundargopal Ghosh[a]**

[a]Department of Chemistry, Indian Institute of Technology Madras, Chennai 600 036, India.

[b]Physical Chemistry Division, CSIR National Chemical Laboratory, Pune, 411008, India.

E-mail: sghosh@iitm.ac.in

Table of contents

I Experimental Details

I. Experimental Details

I.1. Materials and methods

Appropriate perchlorate salts of Na^+, Ca^{2+}, Mg^{2+}, Mn^{2+}, Fe^{2+}, Co^{2+}, Cu^{2+}, Cd^{2+}, Ni^{2+}, Hg^{2+}, Pb^{2+}, (except Zn^{2+} for which triflate salt), ferrocene, hydrazine monohydrate were purchased from aldrich and directly used. Sodium azide, sodium borohydride, acetonitrile (HPLC), diethyl ether, was purchased from local chemicals. Column chromatography was carried out on 3 cm of silica gel in a column of 2.5 cm diameter using 100-200 mesh silica gel. All solvents were dried by conventional methods and distilled under Ar atmosphere before use. Compounds ferrocene mono **2** and dialdehyde **2′**, quinolinehydrazone were synthesized according to literature procedures.[1] UV-vis spectra were taken in CH_3CN/H_2O (1:9) solutions at $c = 1 \times 10^{-5}$ M. Cyclicvoltammetry (CV) was performed with a conventional three-electrode configuration (glassy carbon as working electrode, platinum as auxiliary electrode and Ag/Ag^+ as reference electrode). The experiments were carried out with 10^{-4} M sample solution in CH_3CN using $[(n\text{-}C_4H_9)_4NClO_4]$ (TBAP) as supporting electrolyte, after de-oxygenation of the solution. Working electrode was cleaned at the end of each run. Cyclic voltammograms were recorded at a scan rate 0.1 Vs^{-1}. IR spectrum was recorded using Jasco FT/IR-4100 spectrometer.

The proton conductivities were measured by using a HP4284A impedance analyzer by a quasi-four-probe method in the frequency range 20 Hz to 1 MHz with an applied voltage of 1 V under inert conditions (N2 atmosphere). Impedance data were collected on cylindrical pellets (~10 mm diameter; ~0.9-1.1 mm thickness) obtained by pressing ~0.15 g of sample at 500 MPa for 2 min between porous C electrodes (Sigracet, GDL 10 BB, no Pt). All measurements were electronically controlled by the winDETA package of programs. The electrical measurements were taken in a double-walled, temperature controlled glass chamber with a gas inlet and outlet. The temperature of the chamber was controlled by a Julabo F32-MA refrigerated/heating circulator from 30 to 120 °C every 2 °C with a heating rate of 0.5 $°C\cdot min^{-1}$ using EasyTEMP software. Samples were equilibrated for 15 min after each measurement in a particular temperature in closest vicinity to the sample. The relative humidity (RH) was obtained by a continuous flow of water-saturated nitrogen at different temperatures through the cell. Pellets were equilibrated at 98% RH for 18 h to ensure a fixed water content of the sample and stable conductivity values. RH is approximately constant in the measured temperature range from 30 to 120 °C. Thermogravimetric analysis (TGA) was performed on an SDTQ600 analyzer from TA Instruments. The temperature varied from room temperature to 900 °C at a heating rate of 10 °C•min^{-1}. Measurements were carried out on samples in open platinum crucibles under a flow of air.

I.2. Synthesis

Synthetic procedures of 3 ($C_{22}H_{19}O_2N_3Fe$) and 4 ($C_{34}H_{28}O_4N_6Fe$)

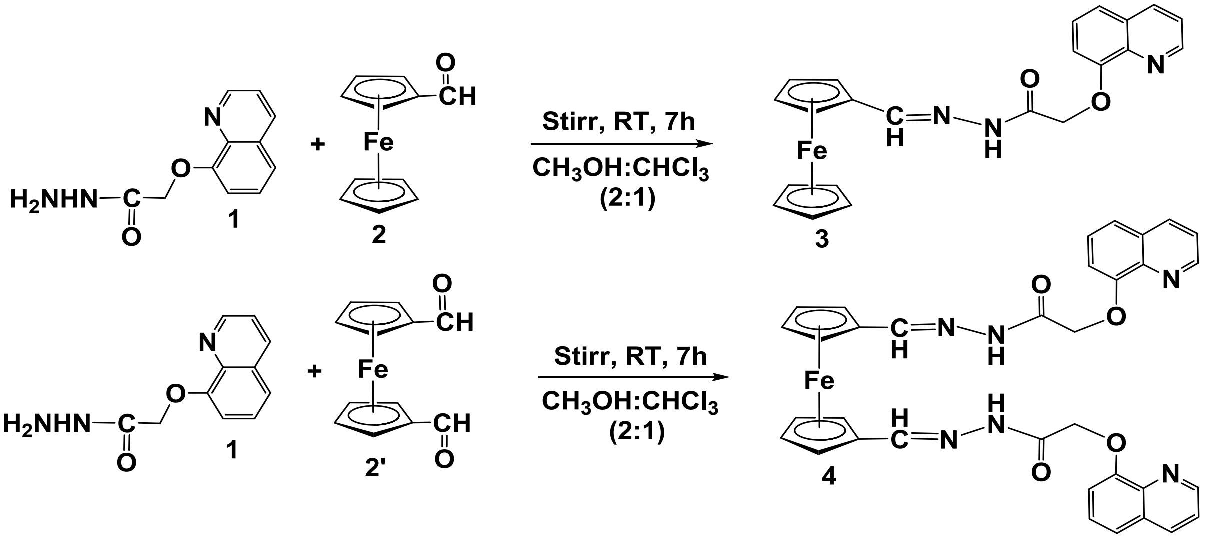

Scheme S1. Synthesis of compounds **3** and **4**.

3 and **4**: To a well–stirred solution of quinolone hydrazone **1** in $CHCl_3$ (0.4g, 0.56 mmol) was added compound **2** (0.138g, 0.56mmole) in CH_3OH and the reaction mixture was stirred at room temperature for 7 hours which yielded a reddish compound **3** (0.39g, 72%). Crude products were purified through silica gel column chromatography by elution with EtOAc/hexane (9:1, v/v). Under the similar reaction conditions, **1** (0.4g, 0.56 mmol) and compound **2**′(0.4g, 0.56 mmol), yielded reddish compound **4** (0.41 g, 75%).

3:^{1}H NMR ($CDCl_3$, 500 MHz): δ = 11.76 (s, 1H, CONH), 8.97 (s, 1H, CH=N), 8.26 (s, 2H, Ar-H), 7.57 (s, 4H, Ar-H), 4.93(s, 2H, -OCH_2), 4.18-4.4(m, 9H, Hcp), ^{13}C NMR ($CDCl_3$, 125 MHz): δ = 150.74, 148.94, 137.16, 127.35, 122.28, 122.09, 113.92, 70.79, 70.63, 69.27, 69.38; IR (KBr, cm-1): 3439, 3229, 2926, 1658, 1394, 1269, 1122, 802, 460; MS(ESI): m/z $[M+H]^+$ for $C_{22}H_{19}O_2N_3Fe$: calculated 413.25; observed 414

4:^{1}H NMR ($CDCl_3$, 500 MHz): δ = 12.37 (s, 2H, 2CONH), 8.96(s, 2H, 2CH=N), 8.19- 8.33(m, 2H, Ar-H), 8.95- 8.96(m, 2H, Ar-H),7.49- 7.51(m, 5H, Ar-H), 7.38- 7.41(m, 3H, Ar-H), 4.63(s, 4H, 2-OCH_2), 4.2-4.34(m, 3H, Hcp), 3.45(s, 5H, Hcp), ^{13}C NMR ($CDCl_3$, 125 MHz): δ = 150.89, 149.06, 136.89, 126.96, 122.18, 121.48, 111.24, 79.28, 71.36, 69. 83, 68.96, IR (KBr, cm-1): 2934, 1690, 1620, 1391, 1120, 805, 463; MS(ESI): m/z $[M+H]^+$ for $C_{34}H_{28}O_4N_6Fe$: calculated 639.46; observed 641

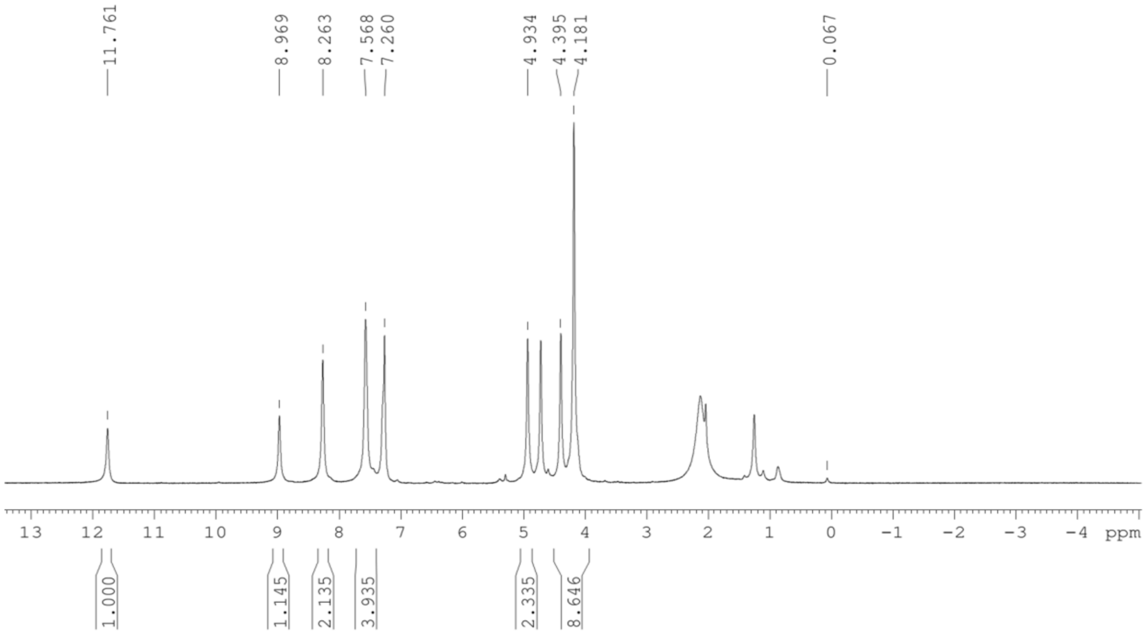

Fig. S1.^{1}H-NMR spectrum of compound **3**

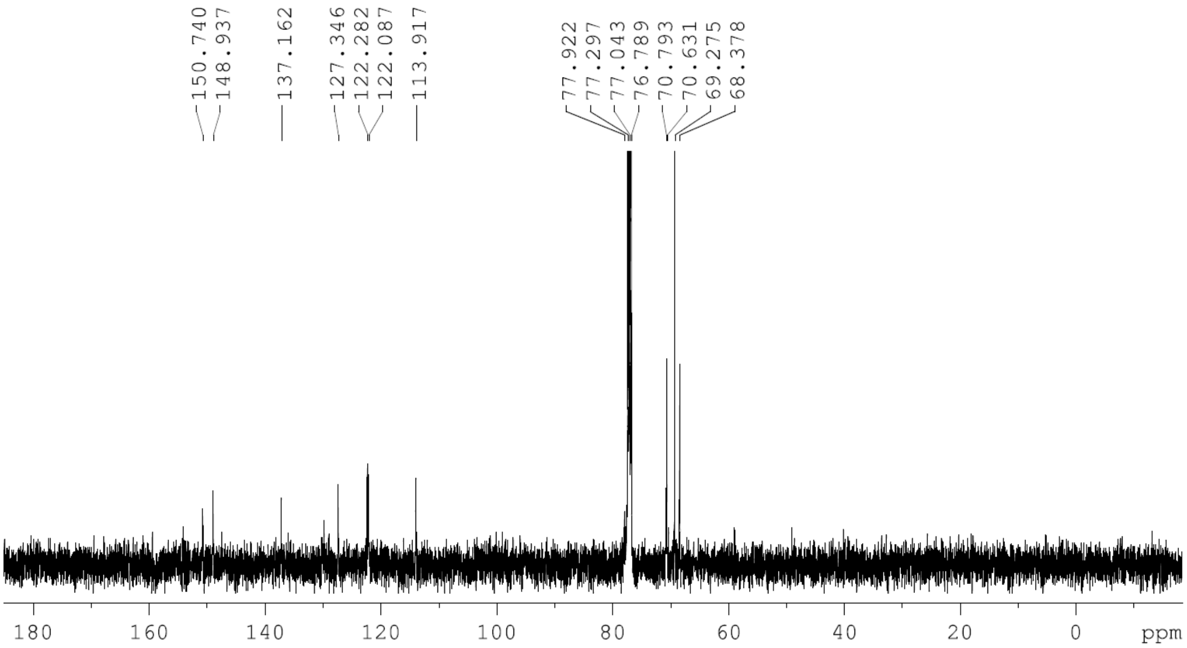

Fig. S2.^{13}C-NMR spectrum of compound **3**

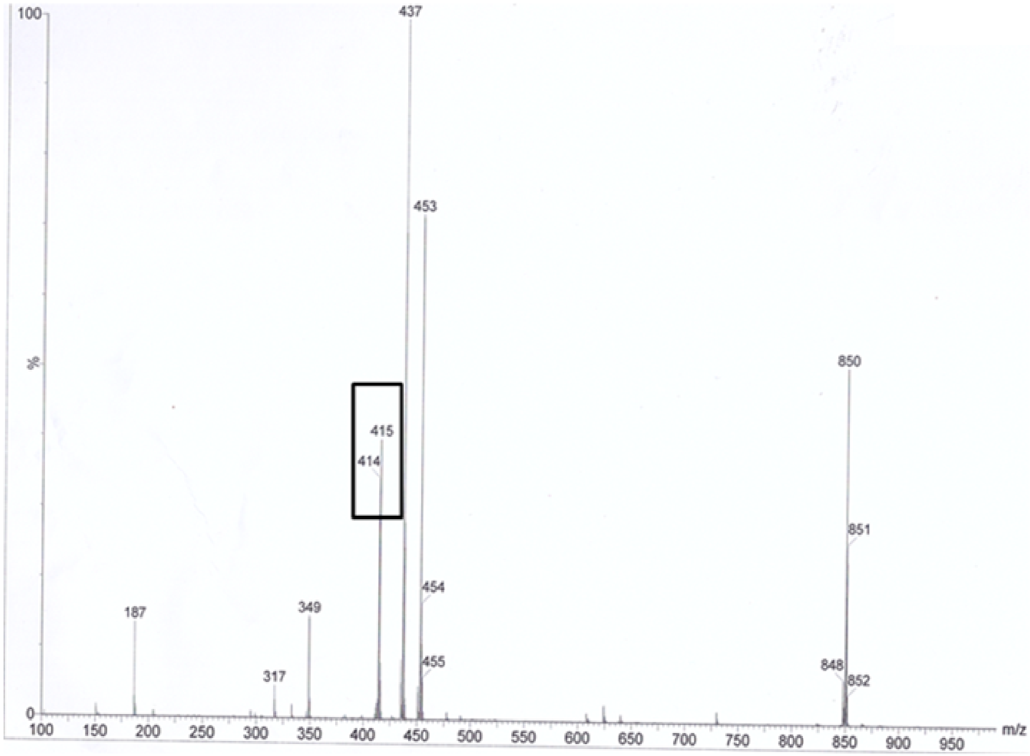

Fig. S3. ESI-mass spectrum of compound **3**

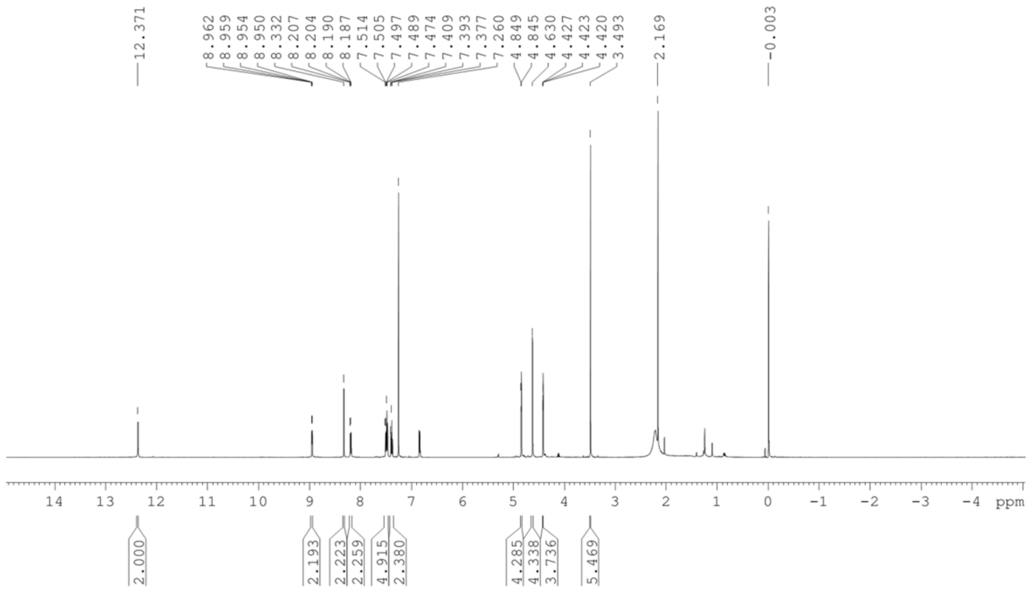

Fig. S4.^{1}H-NMR spectrum of compound **4**

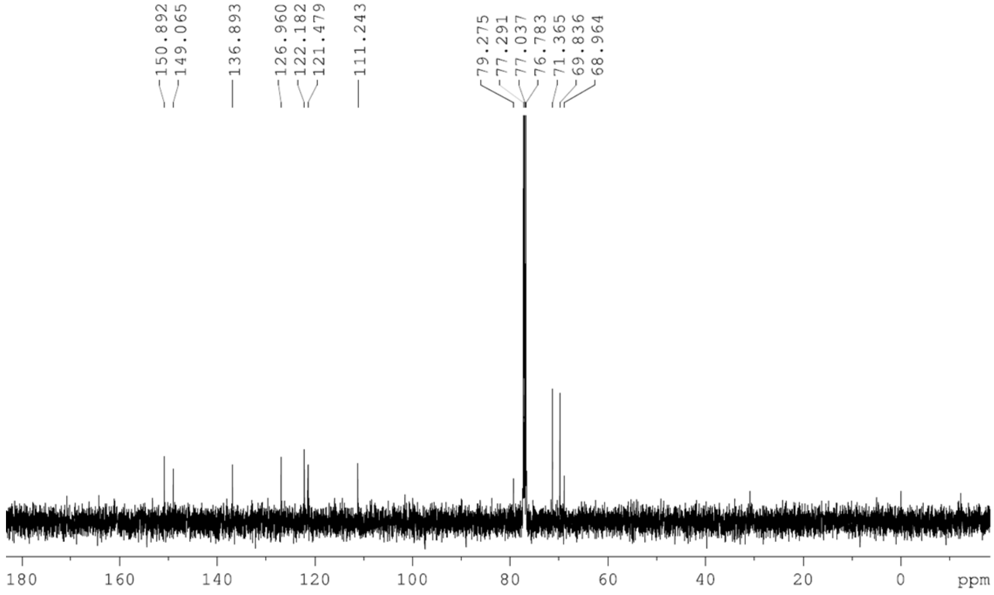

Fig. S5.^{13}C-NMR spectrum of compound **4**

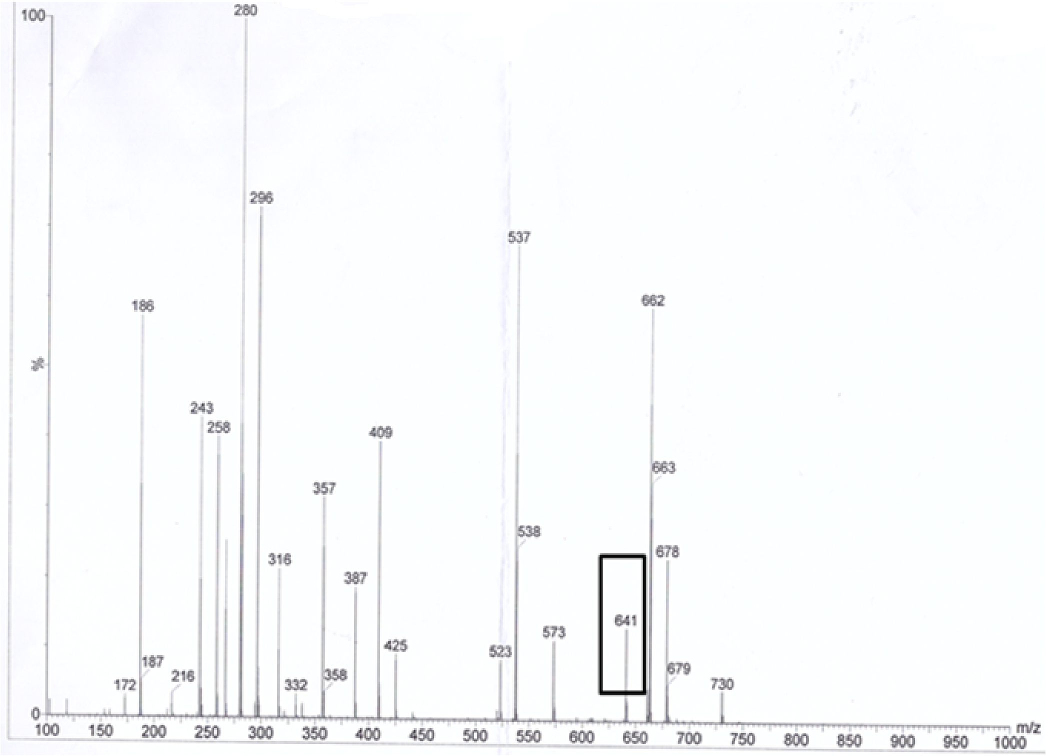

Fig.S6. ESI-mass spectrum of compound **4**

I.3. X-ray Analysis Details

Single crystal X-Ray diffraction and crystal structure of 3:

Suitable X-ray quality crystals of **3** were grown by slow diffusion of a methanol solution and single crystal X-ray diffraction study was undertaken. As-synthesized crystal of **3** was coated with paratone-N and placed on top of a nylon cryoloop (Hampton research) and then mounted in the diffractometer. The data collection was done at 293 K. The crystal was mounted on a Super Nova Dual source X-ray Diffractometer system (Agilent Technologies) equipped with a CCD area detector and operated at 250 W power (50 kV, 0.8 mA) to generate Mo Kα radiation (λ = 0.71073 Å). Initial scans of each specimen were performed to obtain preliminary unit cell parameters and to assess the mosaicity (breadth of spots between frames) of the crystal to select the required frame width for data collection. CrysAlisPro program software was used suite to carry out overlapping φ and ω scans at detector (2θ) settings (2θ = 28). Following data collection, reflections were sampled from all regions of the Ewald sphere to redetermine unit cell parameters for data integration. In no data collection was evidence for crystal decay encountered. Following exhaustive review of collected frames the resolution of the dataset was judged. Data were integrated using CrysAlisPro software with a narrow frame algorithm. Data were subsequently corrected for absorption by the program SCALE3 ABSPACK[2] scaling algorithm.

These structures were solved by direct method and refined using the SHELXTL 97[3] software suite. Atoms were located from iterative examination of difference F-maps following least squares refinements of the earlier models. Final model was refined anisotropically (if the number of data permitted) until full convergence was achieved. Hydrogen atoms were placed in calculated positions (C-H = 0.93 Å) and included as riding atoms with isotropic displacement parameters 1.2-1.5 times Ueq of the attached C atoms. In some cases modeling of electron density within the voids of the frameworks did not lead to identification of recognizable solvent molecules in these structures, probably due to the highly disordered contents of the large pores in the frameworks. Highly porous crystals that contain solvent-filled pores often yield raw data where observed strong (high intensity) scattering becomes limited to ~1.0 Å at best, with higher resolution data present at low intensity. A common strategy for improving X-ray data, increasing the exposure time of the crystal to X-rays, did not improve the quality of the high angle data in this case, as the intensity from low angle data saturated the detector and minimal improvement in the high angle data was achieved. Additionally, diffused scattering from the highly disordered solvent within the void spaces of the framework and from the capillary to mount the crystal contributes to the background and the 'washing out' of the weaker data. Electron density within void spaces has not been assigned to any guest entity but has been modeled as isolated oxygen and/or carbon atoms. The foremost errors in all the models are thought to lie in the assignment of guest electron density. The structure was examined using the *ADSYM* subroutine of PLATON[4] to assure that no additional symmetry could be applied to the models. The ellipsoids in ORTEP diagrams are displayed at the 50% probability level.

Crystal data for **3**: CCDC 1018549, $C_{22}H_{23}O_4N_3Fe$, Mr = 449.28, Monoclinic space group P21/c, a = 14.9238(15) Å, *b* = 19.0060(16) Å, c = 7.3188(7) Å, $\alpha = 90.00°$, $\beta = 99.41(11)°$, $\gamma = 90.00°$, V = 2048.0(3)Å, Z = 4, ρcalcd = 1.457 $mg \cdot mm^{-3}$, μ = 0.771 mm^{-1}, F(000) = 936, R_1 = 0.0340, wR_2 = 0.1305, 4613 independent reflections [$2\theta \leq 58.2°$] and 277 parameters

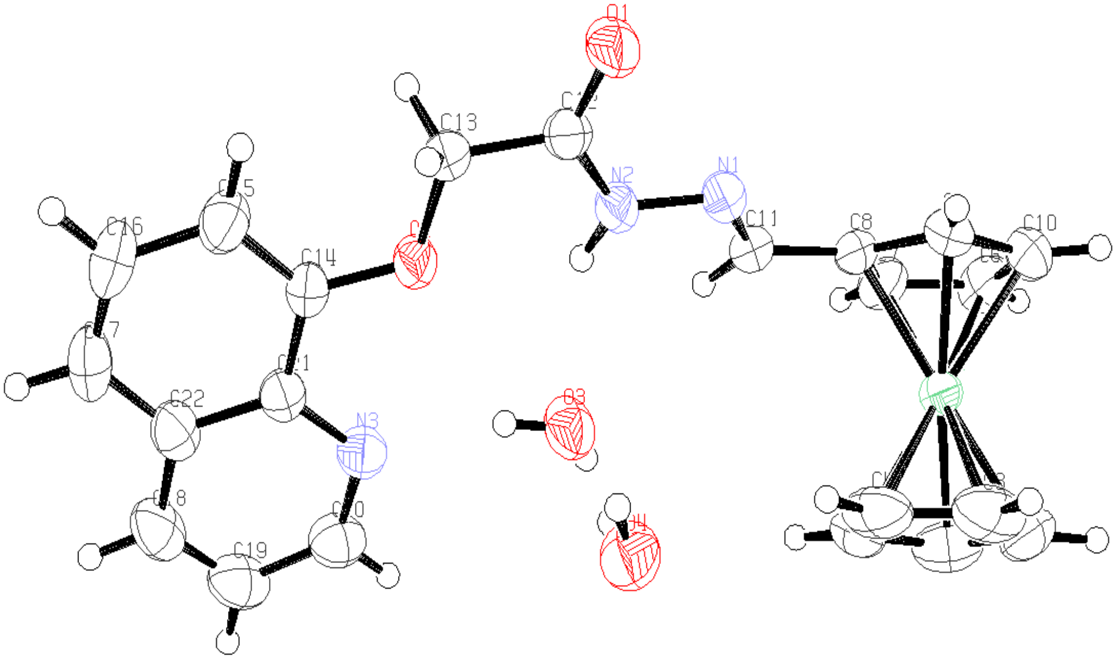

Fig. S7. ORTEP drawing of **3**. (thermal ellipsoids set to 50% probability level)

Single crystal X-Ray diffraction and crystal structure of 4:

Suitable X-ray quality crystals of **4** were grown by slow diffusion of a hexane: EtOAc (6:4 *v/v*) solution and single crystal X-ray diffraction study was undertaken. X-ray single crystal data were collected using Mo Kα (λ = 0.71073 Å) radiation on BRUKER APEX II diffractometer equipped with CCD area detector. Data collection, data reduction, structure solution/refinement were carried out using the software package of SMART APEX. The solid state structure of compound **4** was solved by direct method and refined in a routine manner.

Crystal data for **4**: CCDC 1018535, $C_{34}H_{36}O_6N_6Fe$, Mr = 704.56, Triclinic space group P -1, *a* = 10.6299(4) Å, *b* = 11.4199(4) Å, c = 14.0961(5) Å, α = 101.1842(17)°, β = 104.9276(17)°, γ = 94.4000(18)°, V = 1607.46(10)Å, Z = 2, ρcalcd = 1.456 mg mm^{-3}, μ = 0.527 mm^{-1}, F(000) = 736, R_1 = 0.0408, wR_2 = 0.0818, 5658 independent reflections [2θ≤49.99°] and 460 parameters.

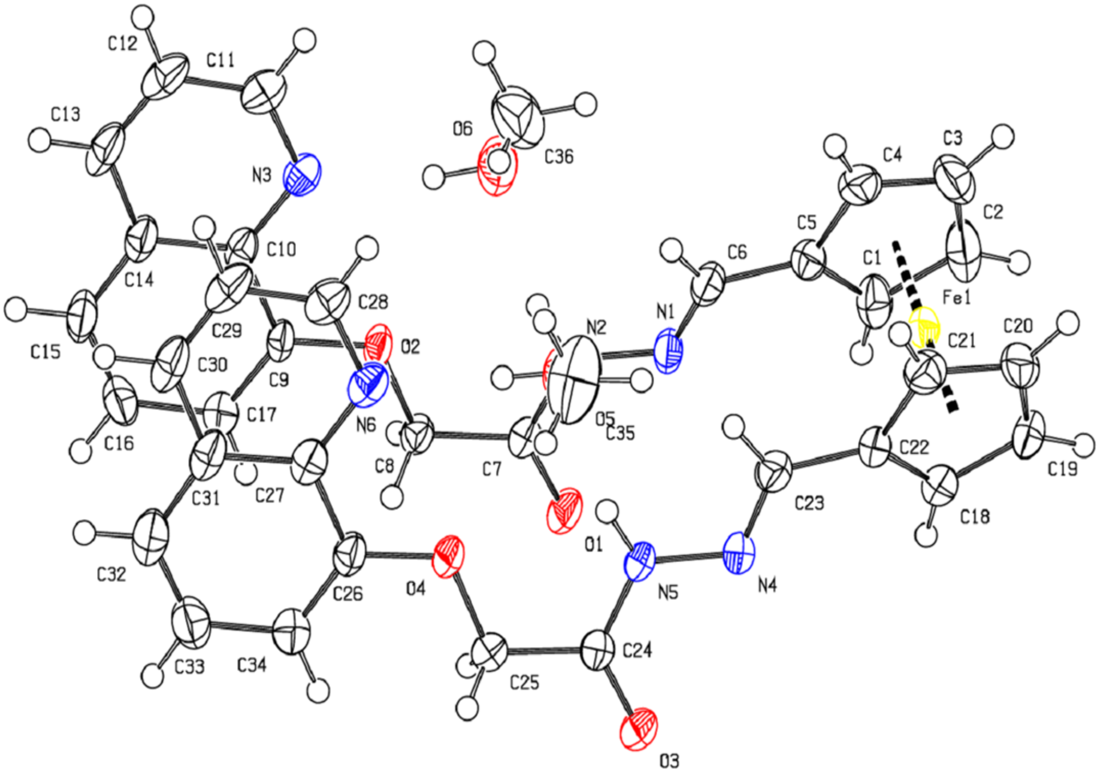

Fig. S8. ORTEP drawing of **4**. (thermal ellipsoids set to 50% probability level)

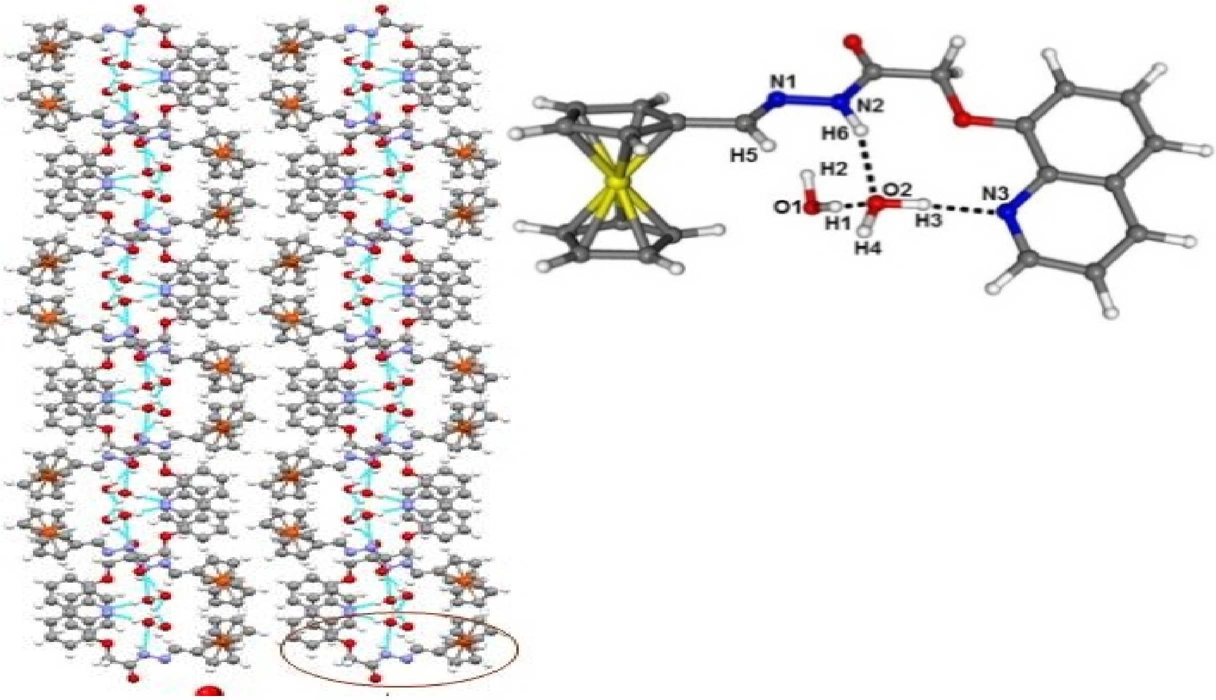

Fig. S9. 3D packing structure of the undulated layers of **3** viewed along the *c* axis where hydrogen bonding interactions are arranged the lattice water molecules in 1D helical manner (left), hydrogen bonding contacts between the lattice water molecules and nitrogen atoms in compound **3** (right).

Crystal structure analysis of compound 4:

Figure S10 shows the perspective view of **4**. The asymmetric unit of **4** contains one independent [$Fe_1C_{34}O_4N_6H_{28}$] molecule and two CH_3OH solvent molecules. The 3D supramolecular architecture shows that the molecules are arranged as separate walls. The fascinating aspect of the structure is the encapsulation of solvent methanol molecules along the zigzag networks in the form of hydrogen bonds and intermolecular interactions.[5] H-bonding and the π-π stacking interactions are the dominant interactions in the solid state X-ray structure structure of **4**.

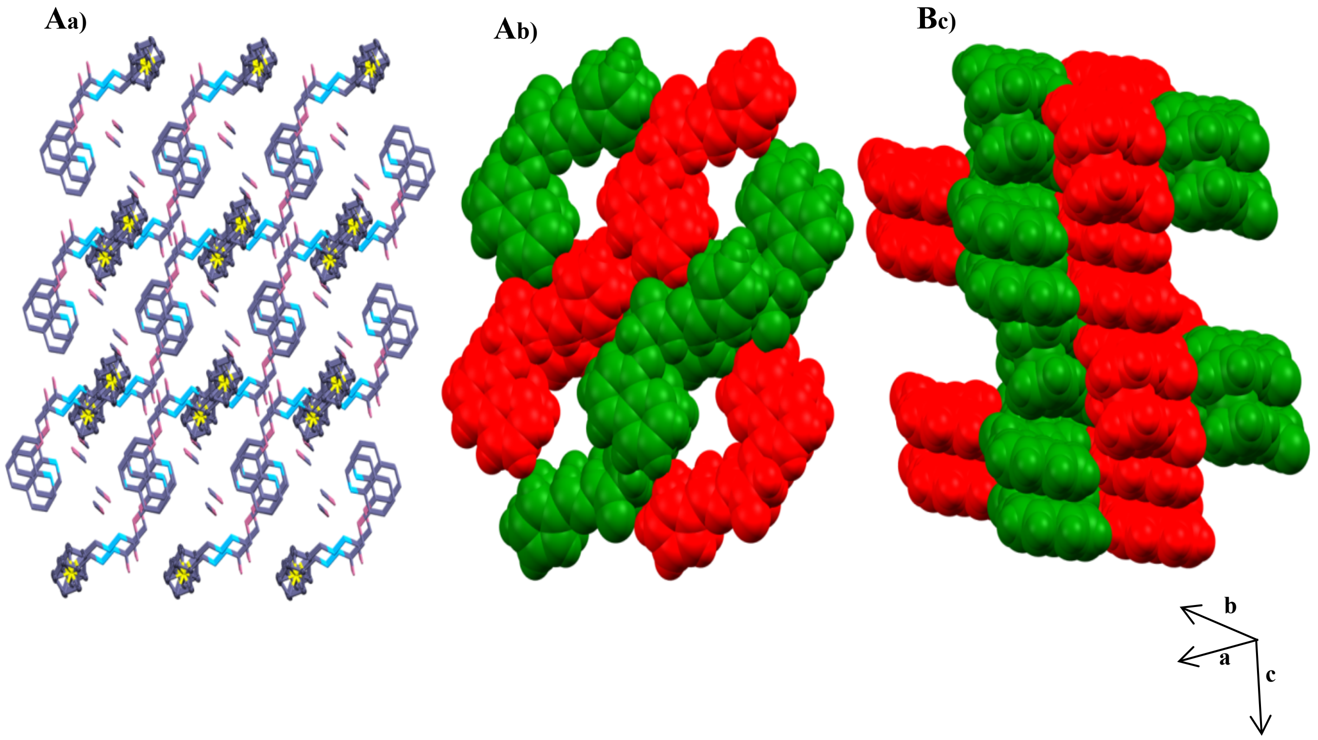

Fig. S10. (a) 3D packing structure of the undulated layers of **4** viewed along the c axis, (hydrogen atoms are omitted for clarity) Color code: Fe: yellow; C: violet; N: cyan; O: scarlet red; (b) space-filling graphic of 3D packing structure along c axis;(c) another 3D perspective view. Note the channel voids that are accommodated by the methanol crystallization solvent (omitted).

From a topological point of view, compound **4** features an interesting 1D zigzag network sustained by π-π stacking and weak interactions (Fig. S11). It is worth noting that the quinoline groups of two inversion related molecules in **4** are exactly parallel and display pairwise π–π stacking interactions (Fig. S11). Along with other interactions, π–π interaction is one of the major reasons for the supramolecular architecture of this molecule which can be visualized as steps. The moieties of one pair are related to another through an inversion center located between the quinoline groups. The interplanar separation between the two quioline groups present within the molecule is 3.69 Å and between the two neighboring quinoline groups of adjacent enantiomeric molecules is 3.35 Å. As a result of strong π-π stacking, the molecules are arranged in sheets parallel to the ab plane in an ABAB... fashion, as shown in (Fig. S11).

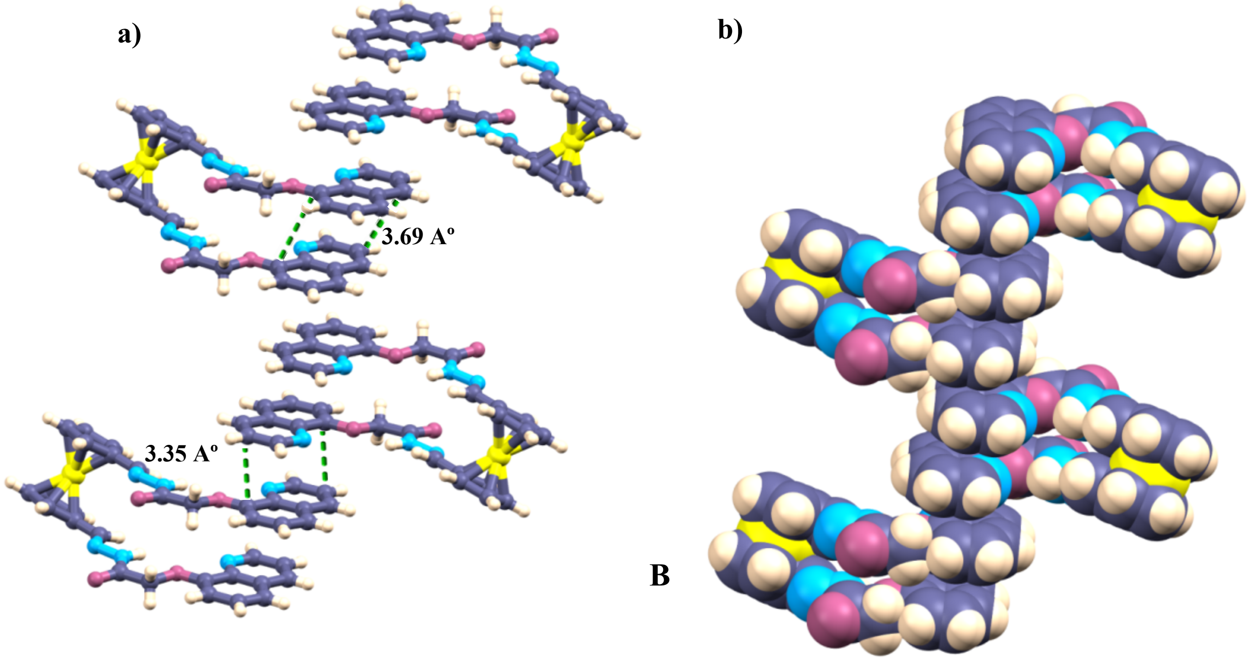

Fig. S11 (a) Zigzag-shaped π–π stacking interactions of **4** along a axis making parallel sheets; (b) space filling illustration of the crystal packing in **4**, viewed along the a axis (all CH_3OH molecules are omitted for clarity), Color code: Fe: yellow; C: violet; N: cyan; O: scarlet red; H: golden yellow.

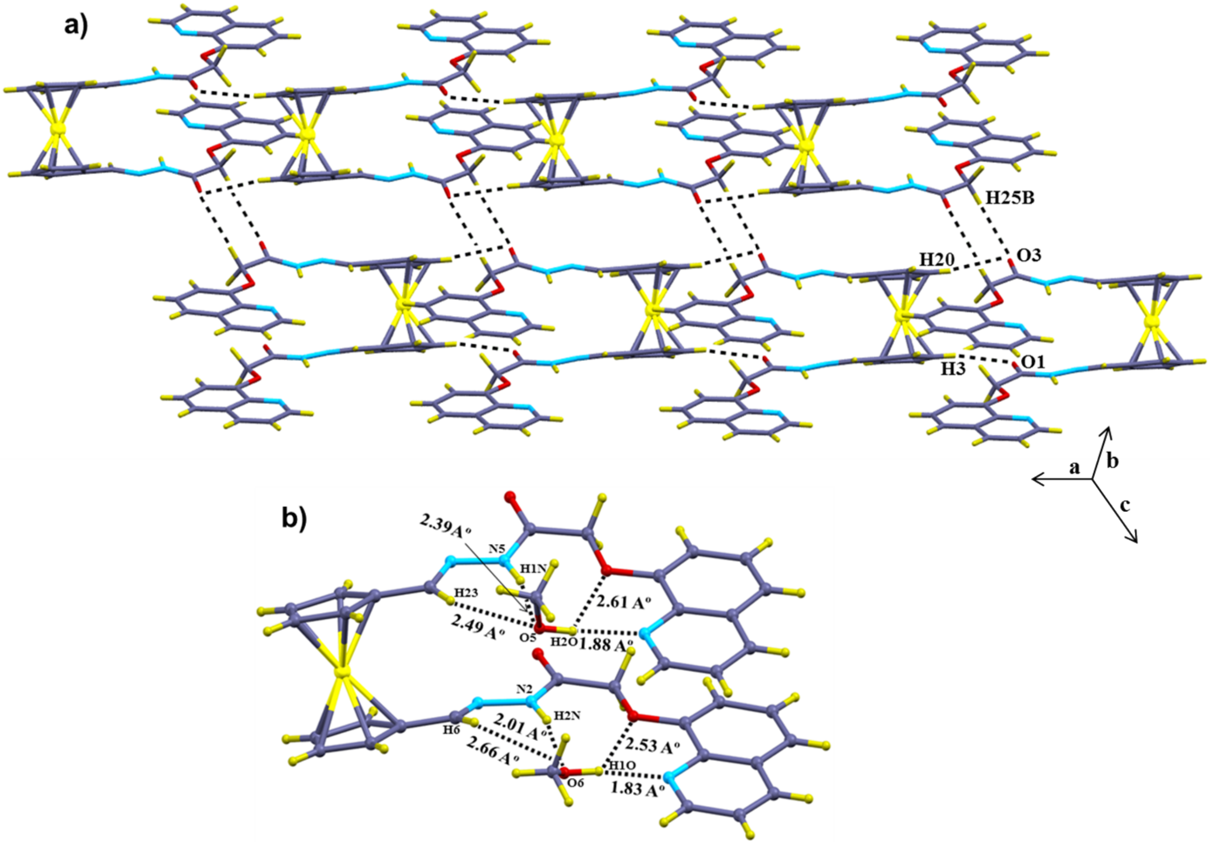

Fig. S12. (a) C-H···O interaction between the adjacent layered molecular units of **4** in parallel to the ac-plane of the crystal (solvent molecule removed for clarity), Color code: Fe: yellow; C: violet; N: cyan; O: scarlet red; H: light green. (b) The hydrogen bonding pattern between parent molecule and the solvent methanol molecules present in the lattice; Color code: Fe: yellow; C: violet; N: cyan; O: scarlet red; H: light green.

II. Supplementary Data

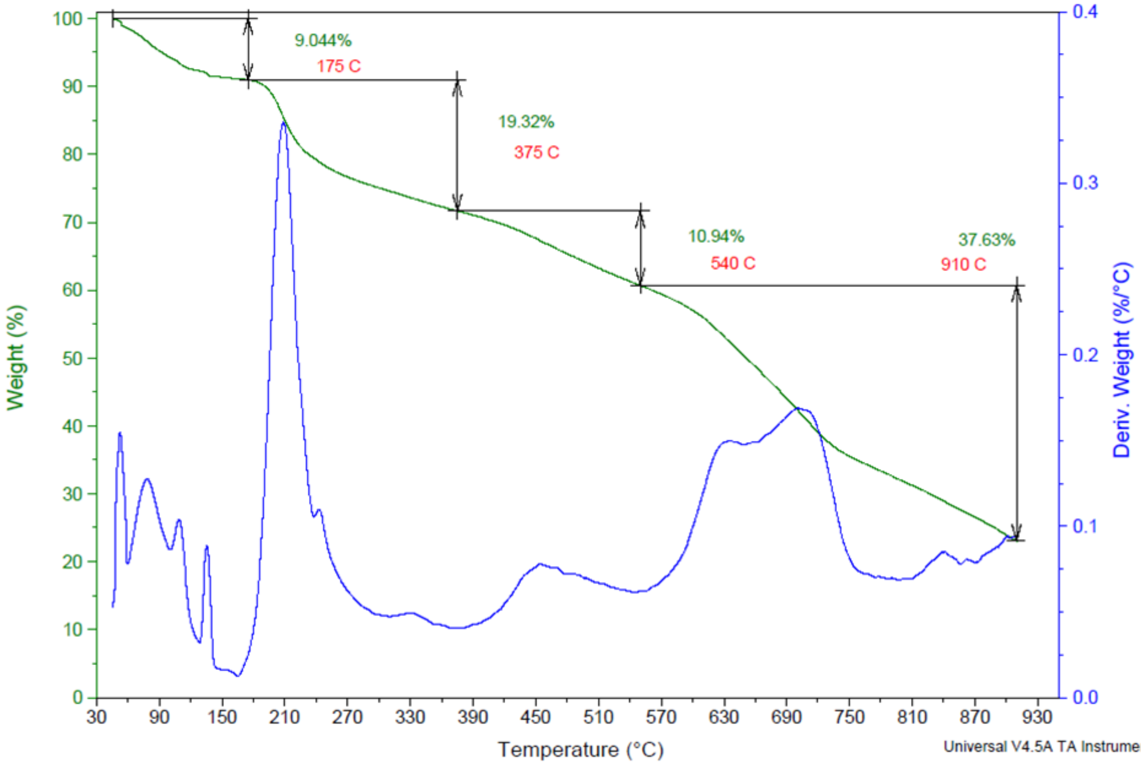

Fig. S13. Thermal Gravimetric Analysis (TGA) of compound **3**

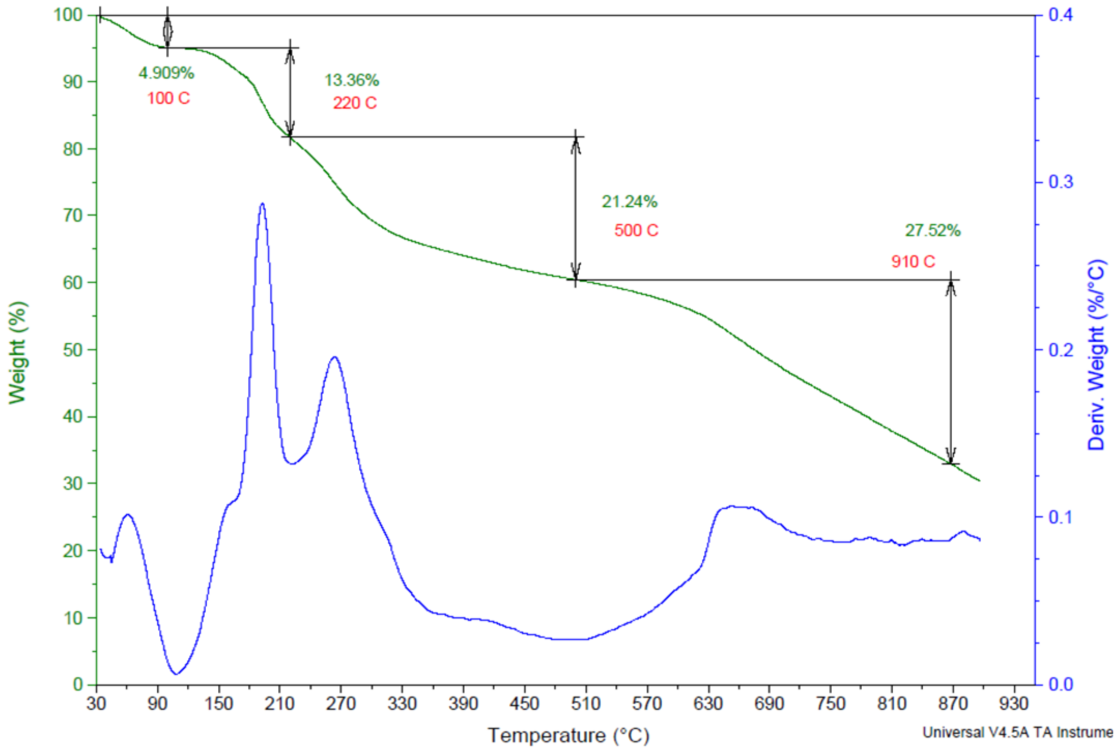

Fig. S14. Thermal Gravimetric Analysis (TGA) of compound **4**

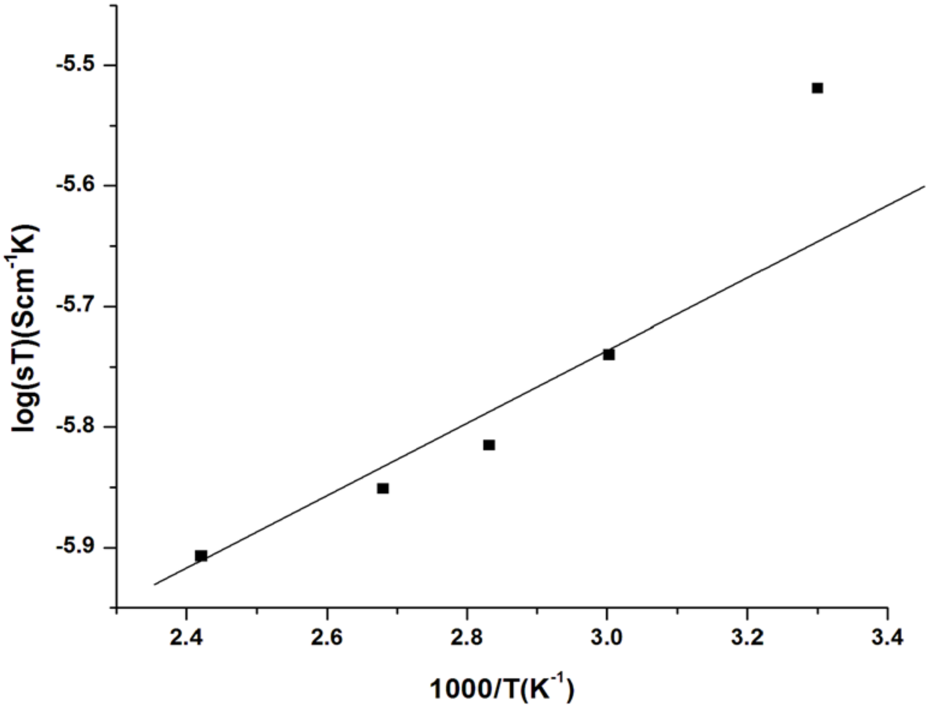

Fig. S15. Arrhenius plots of proton conductivity of compound **3**

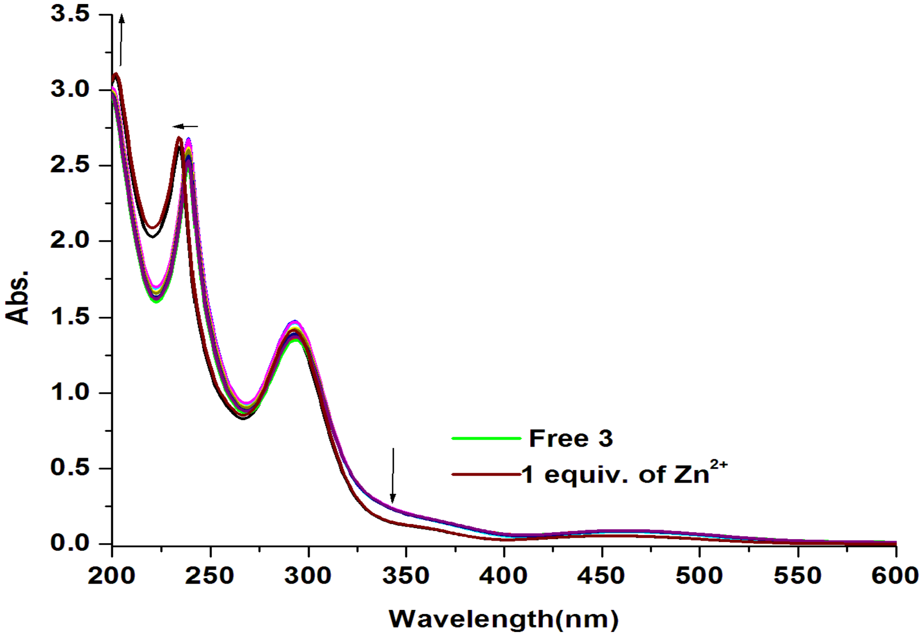

Fig. S16. UV-vis absorption spectra of **3** (10^{-5} M) upon addition of Zn^{2+} ion up to 1 equivalent in CH_3CN/H_2O (1/9)

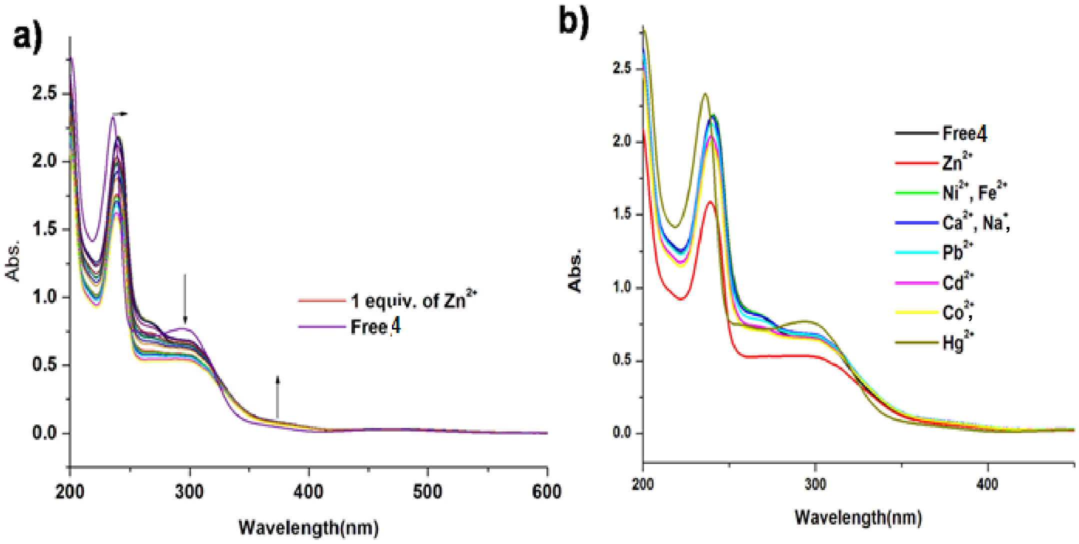

Fig. S17. UV-vis absorption spectra of **4** (10^{-5} M) upon addition of Zn^{2+} ion up to 1 equivalent in CH_3CN/H_2O (1/9).

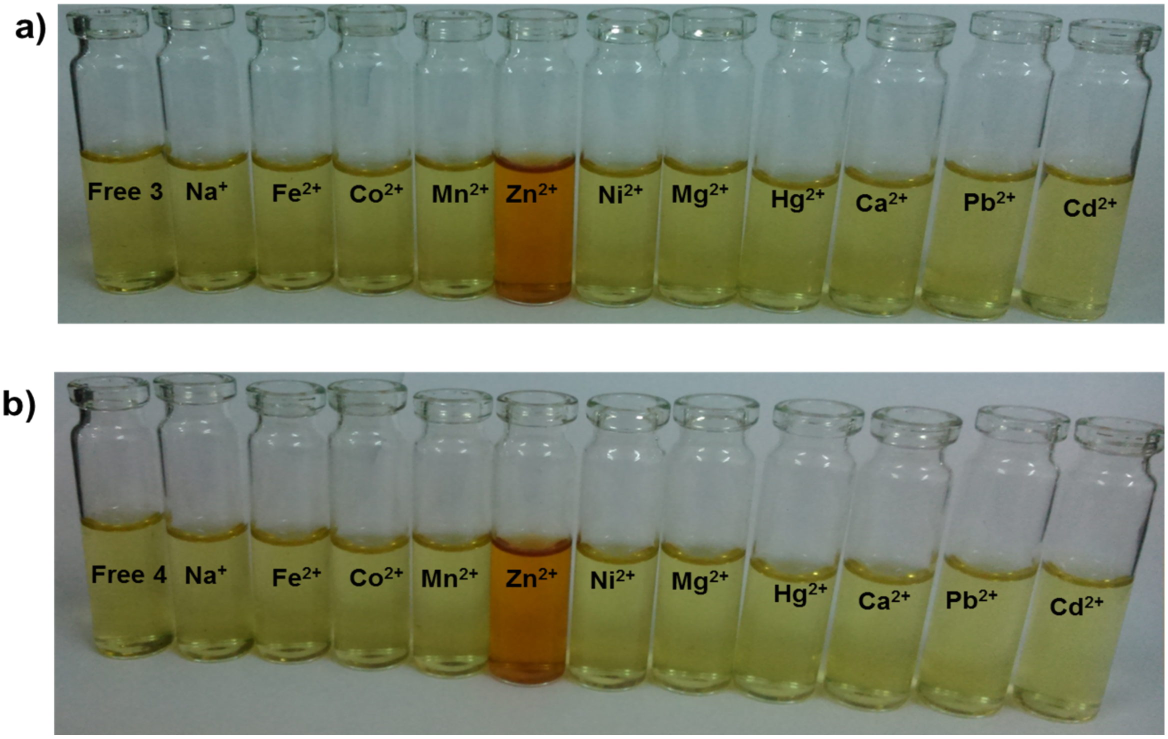

Fig. S18. Evolution of the color in CH_3CN solution of **3** (10^{-5} M) (top) and **4** (down) after addition of 5 equivalents of different cations tested as perchlorate salts.

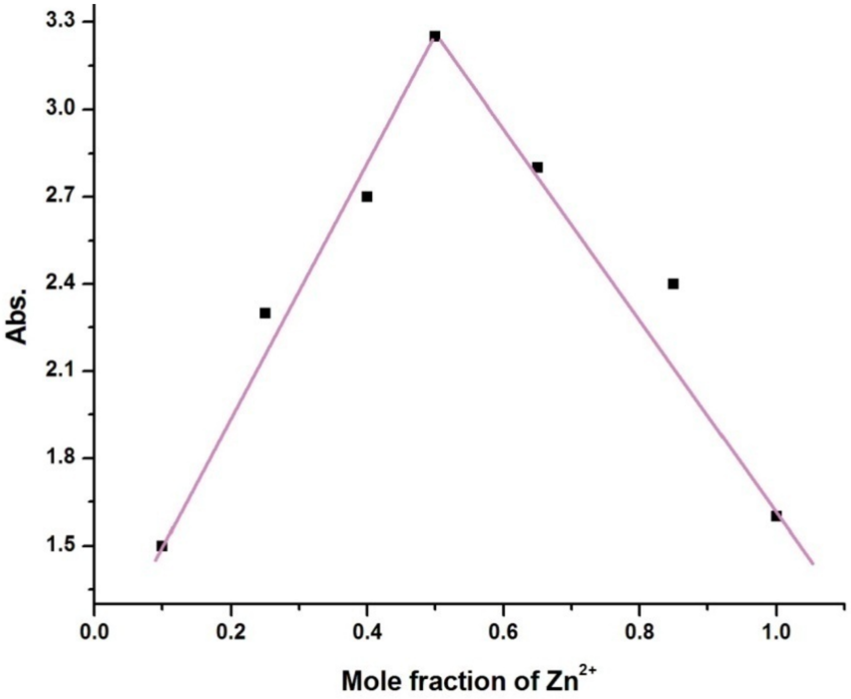

Fig. S19. Job's plot for compounds **3** in presence of Zn^{2+} ion.

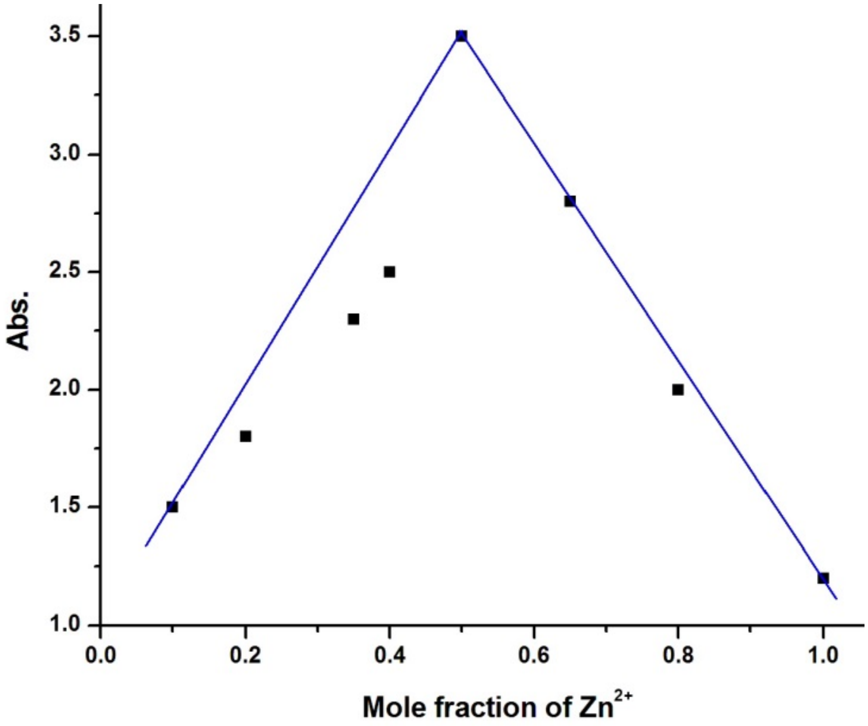

Fig. S20. Job's plot for compounds **4** in presence of Zn^{2+} ion

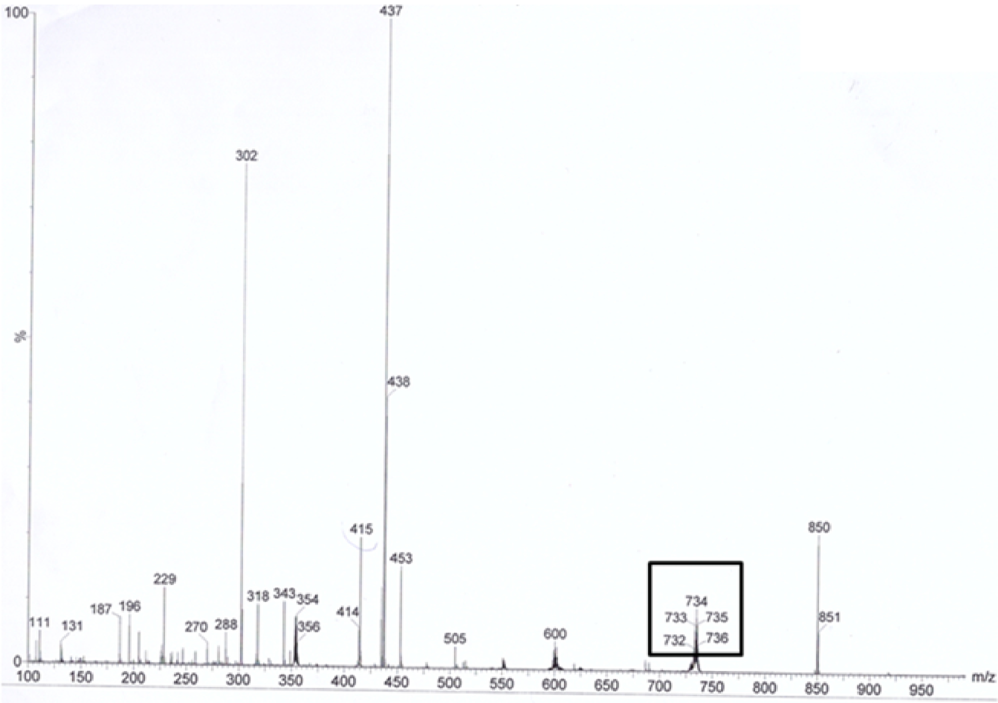

Fig. S21. ESI-mass spectrum of **3.**[Zn^{2+}]

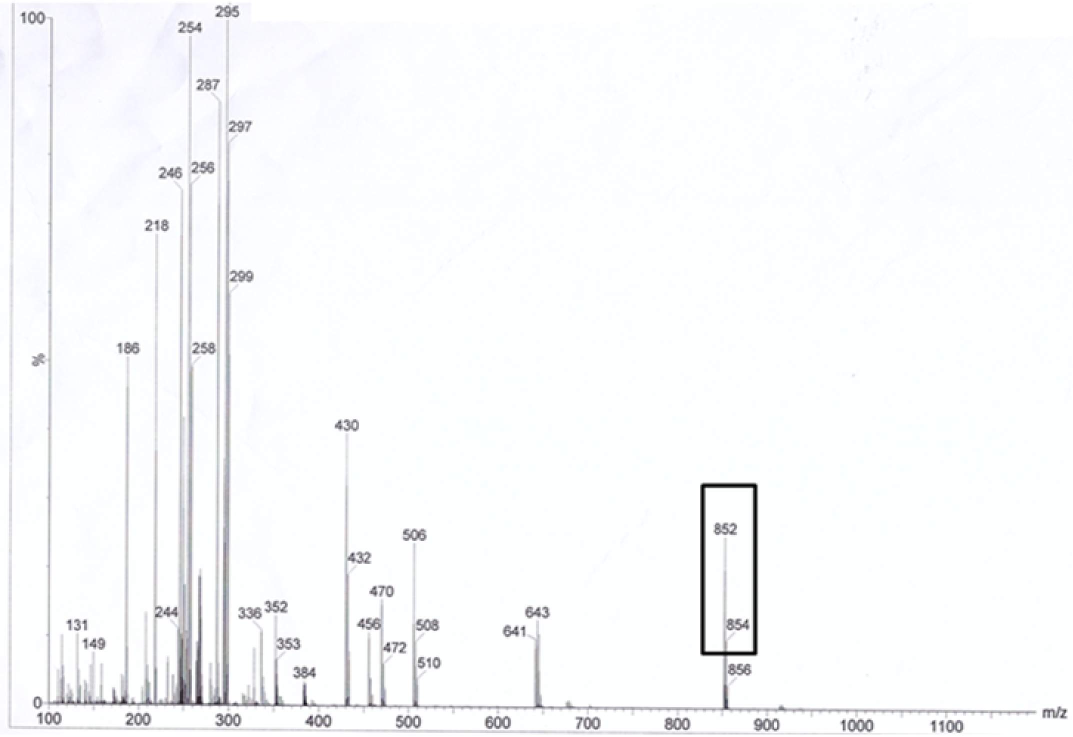

Fig. S22. ESI-mass spectrum of **4.**[Zn^{2+}]

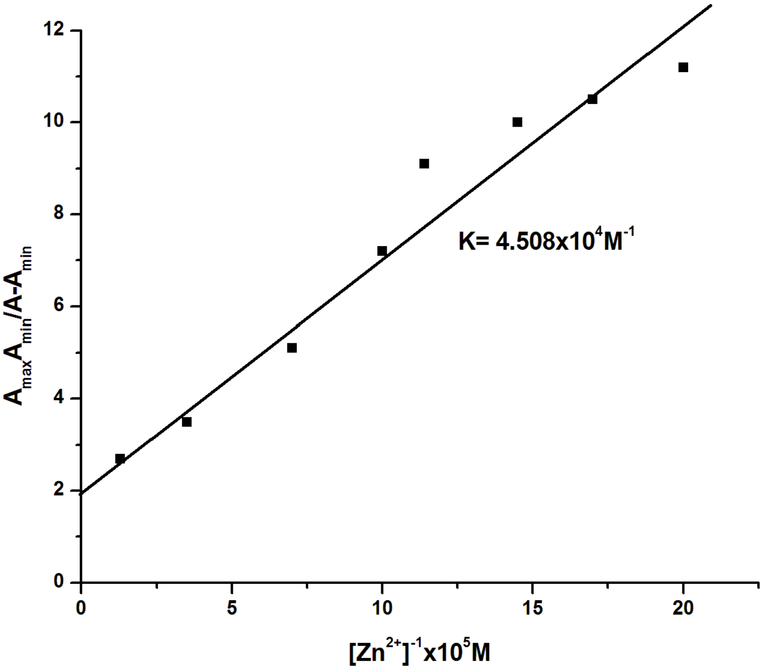

Fig. S23. Quantitative binding data (Benesi-Hildebrand plot) for **3** with Zn^{2+} ion

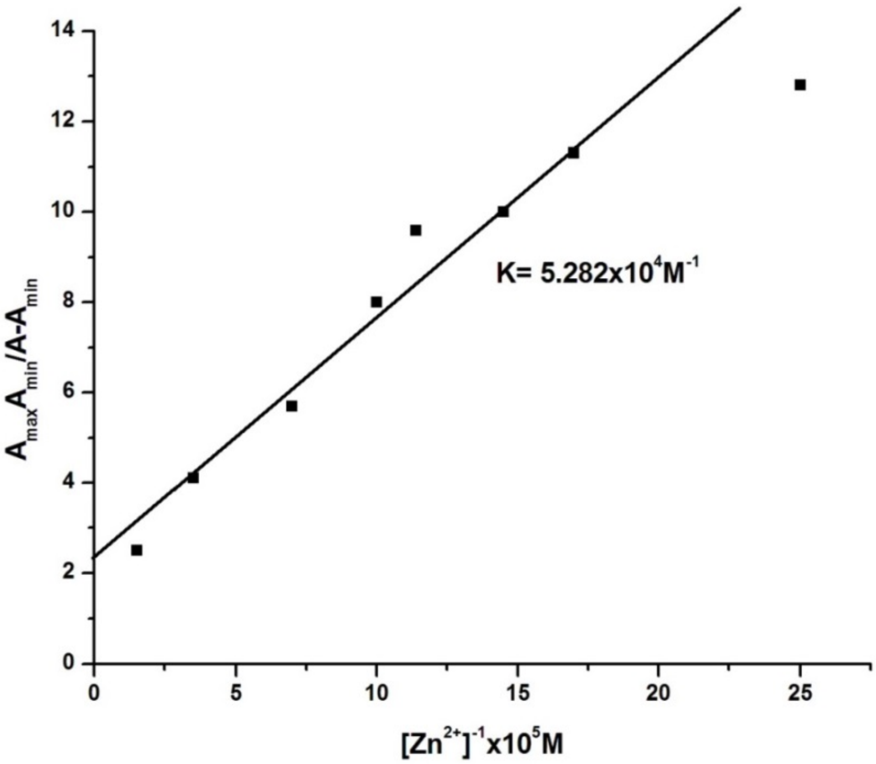

Fig. S24. Quantitative binding data (Benesi-Hildebrand plot) for **4** with Zn^{2+} ion

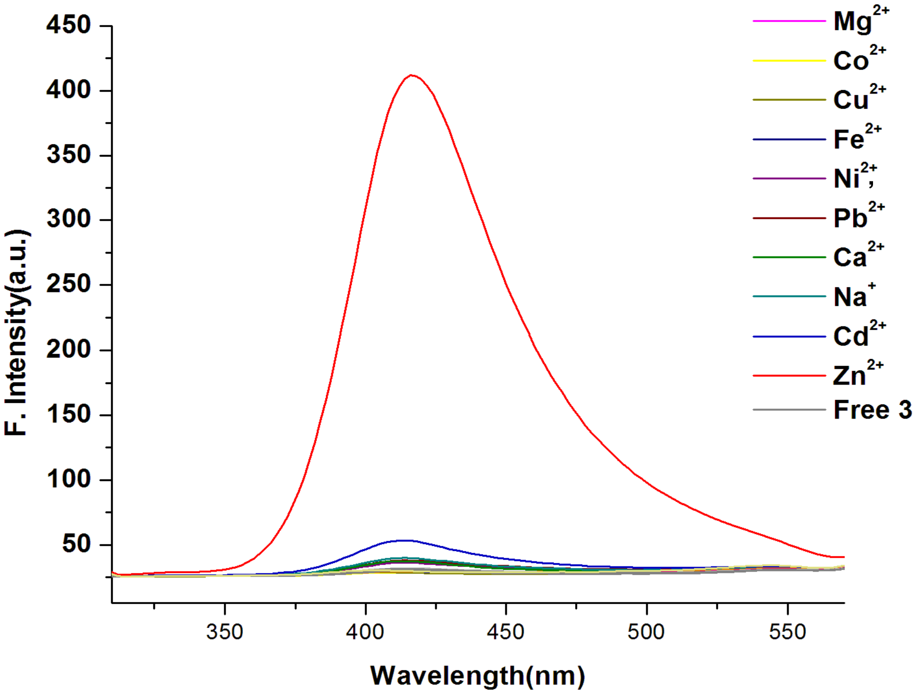

Fig. S25. Changes in the fluorescence spectrum of **3** (1 x 10^{-5} M) in CH_3CN/H_2O (1:9) upon addition of several metal cations

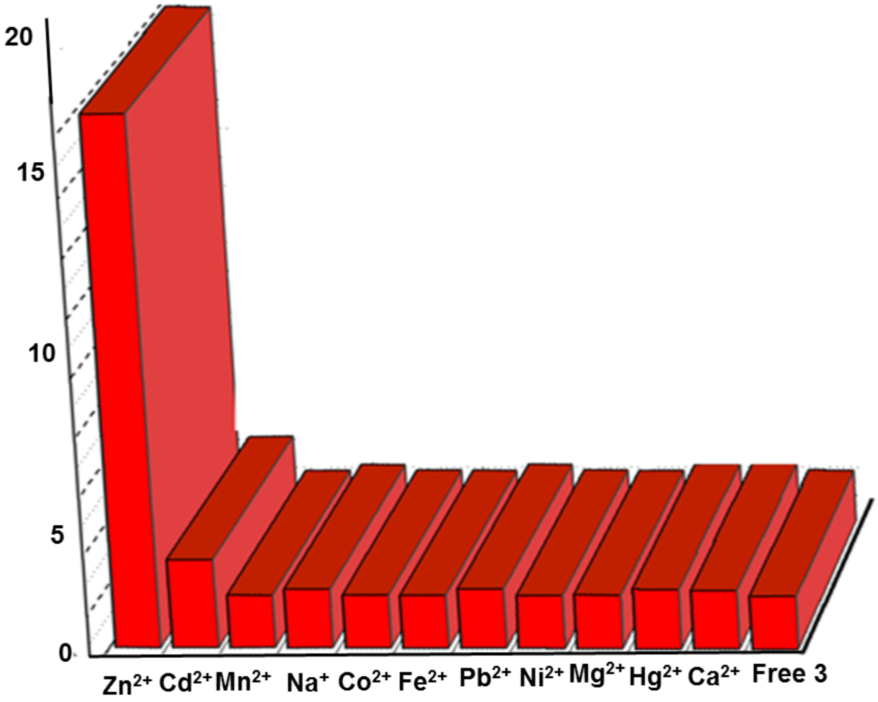

Fig. S26. A bar diagram of the relative maximum intensity of the ligand **3** upon addition of several cations.

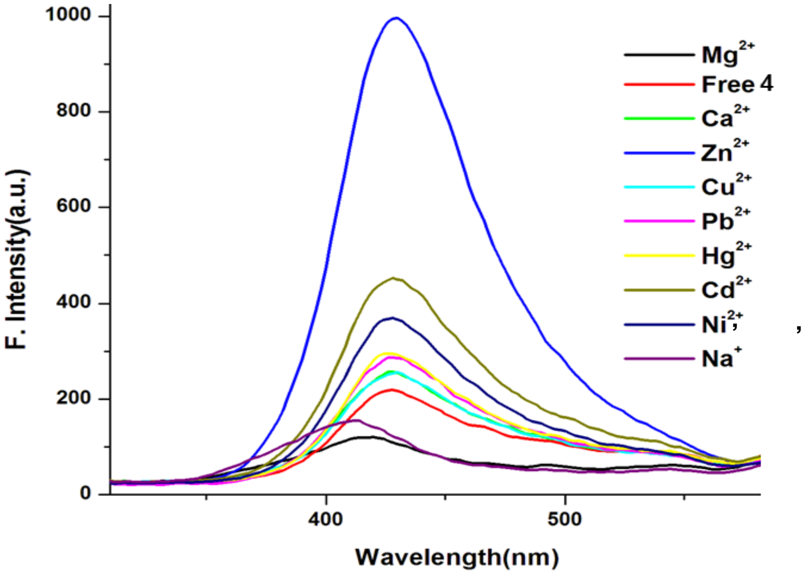

Fig. S27. Changes in the a fluorescence spectra of **4** (1×10^{-5} M) in CH_3CN/H_2O (1:9) upon addition of several metal cations

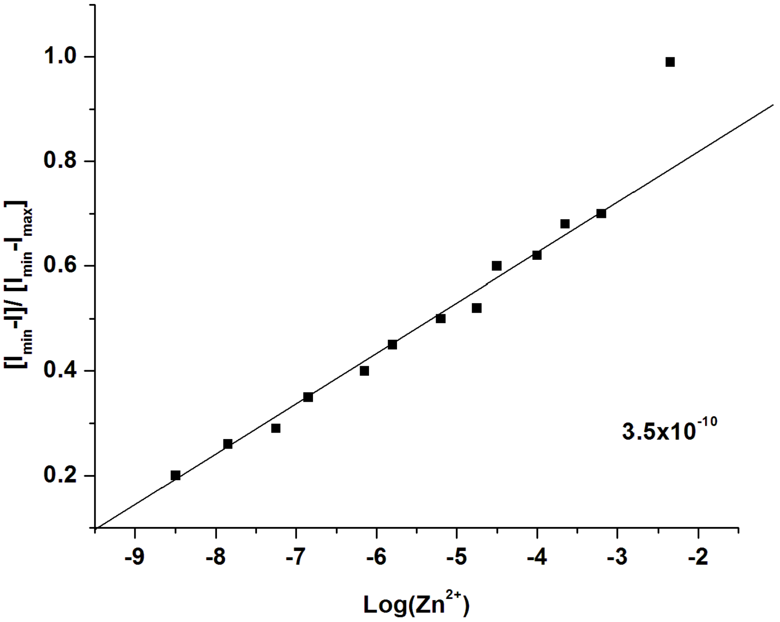

Fig. S28. Fluorescence intensity of **3** at each concentration of Zn^{2+} added normalized between the minimum fluorescence intensity and the maximum fluorescence intensity.

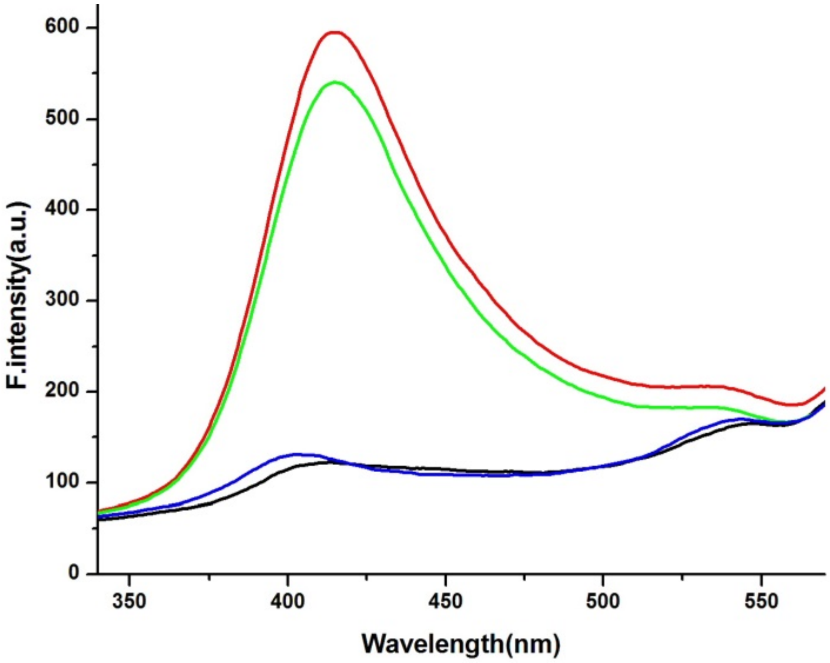

Fig. S29. Reversibility interaction between **3** and Zn^{2+} by extraction method in CH_2Cl_2. Fluorescence spectrum of the free ligand **3** (blue), after the complexation with Zn^{2+} ion (red) and after extraction with water (black) shows the reversibility of the complexation process.

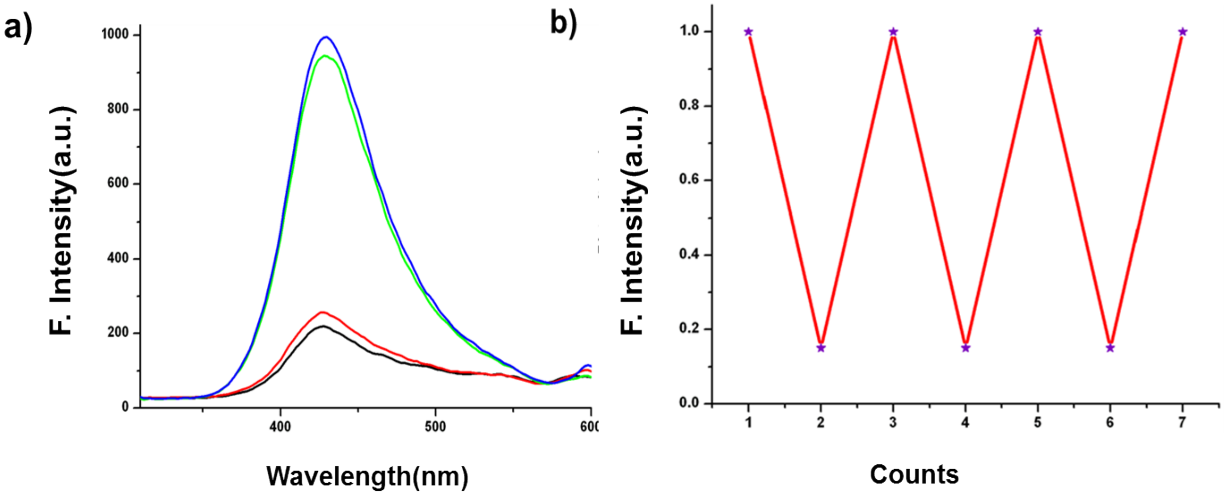

Fig. S30. (a) Reversibility interaction between **4** and Zn^{2+} by extraction method in CH_2Cl_2. Fluorescence spectrum of the free ligand **4** (red), after the complexation with Zn^{2+} ion (blue) and after extraction with water (black) shows the reversibility of the complexation process; (b) Stepwise complexation/decomplexation cycles carried out in CH_3CN/H_2O (5/5) with **4** and Zn^{2+}.

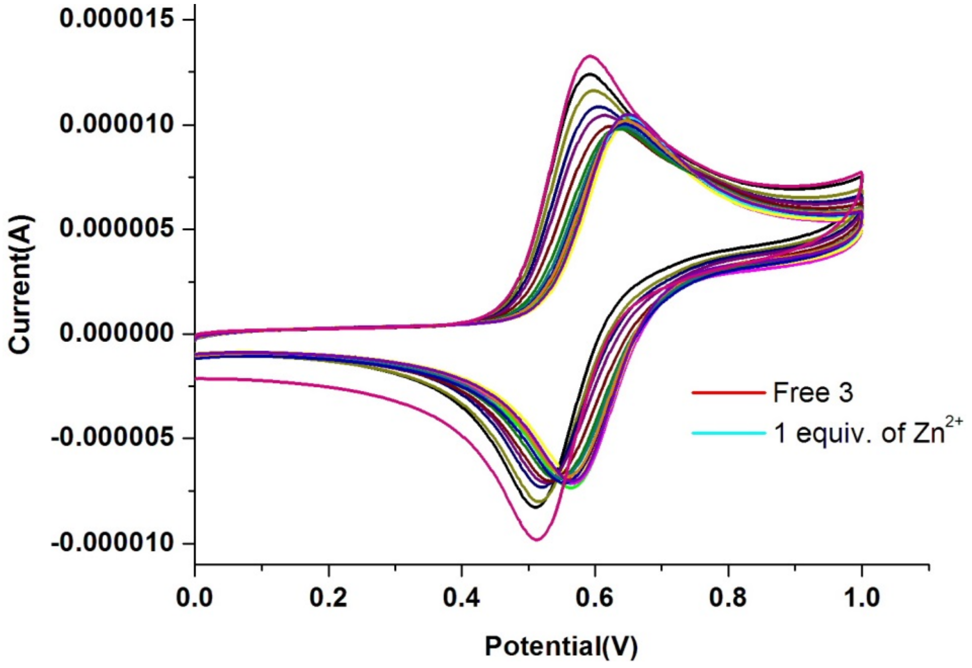

Fig. S31. Evolution of CV of **3** ($1x10^{-4}$ M) upon addition of Zn^{2+} up to 1 equivalent with $[(n-Bu)_4N]ClO_4$ as supporting electrolyte. Scan rate employed 0.1 VS^{-1}

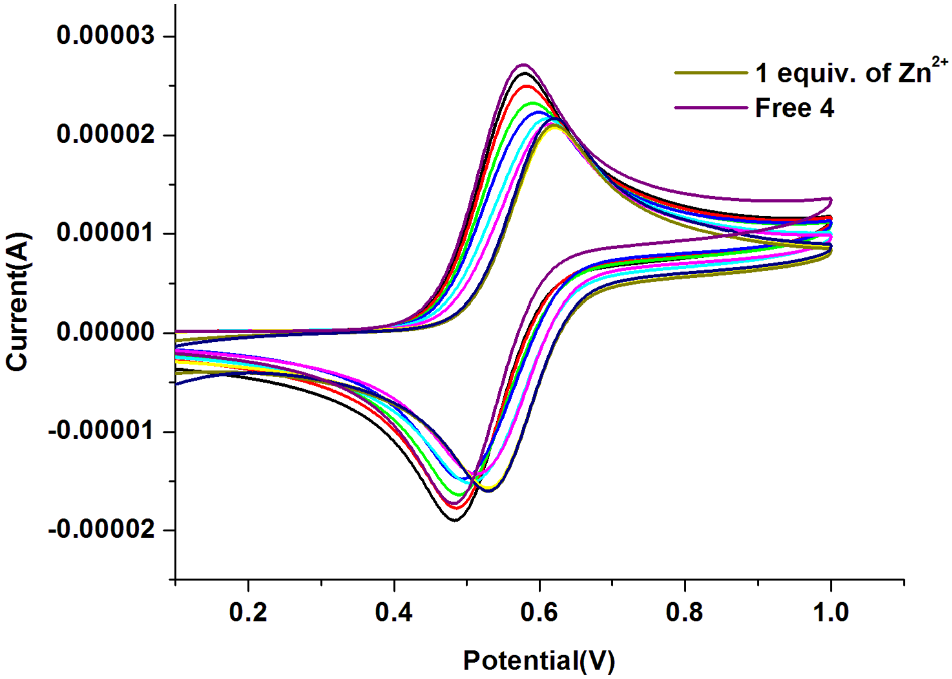

Fig. S32. Evolution of CV of **4** ($1x10^{-4}$ M) upon addition of Zn^{2+} up to 1 equivalent with $[(n-Bu)_4N]ClO_4$ as supporting electrolyte. Scan rate employed 0.1 VS^{-1}

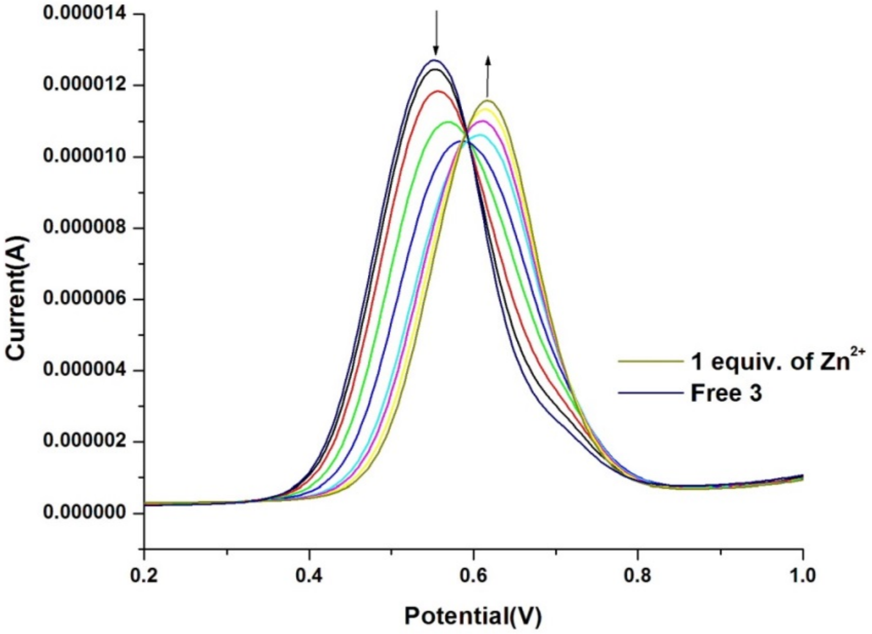

Fig. S33. Evolution of DPV of **3** ($1x10^{-4}$ M) upon addition of Zn^{2+} up to 1 equivalent with $[(n\text{-}Bu)_4N]ClO_4$ as supporting electrolyte. Scan rate employed 0.1 VS^{-1}

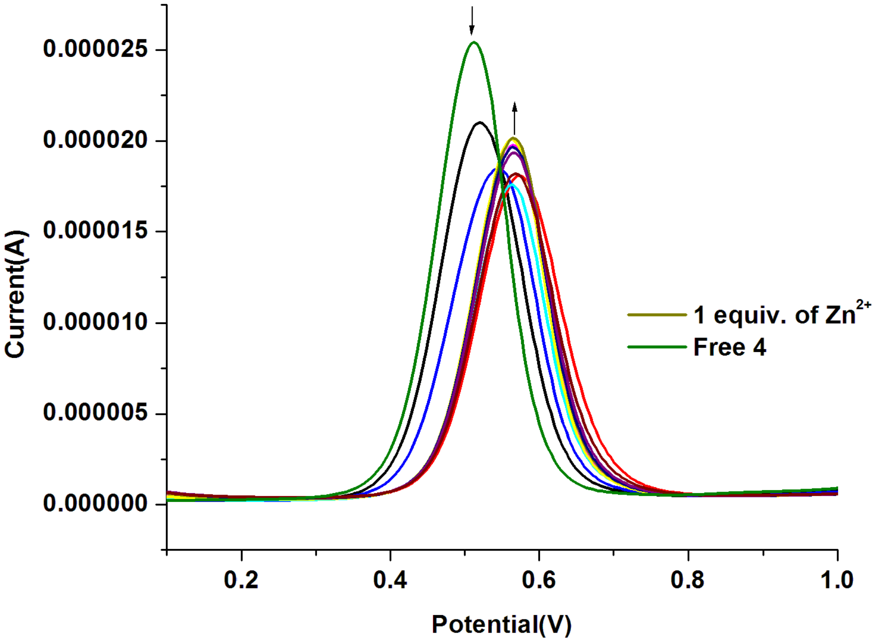

Fig. S34. Evolution of DPV of **4** ($1x10^{-4}$ M) upon addition of Zn^{2+} up to 1 equivalent with $[(n\text{-}Bu)_4N]ClO_4$ as supporting electrolyte. Scan rate employed 0.1 VS^{-1}.

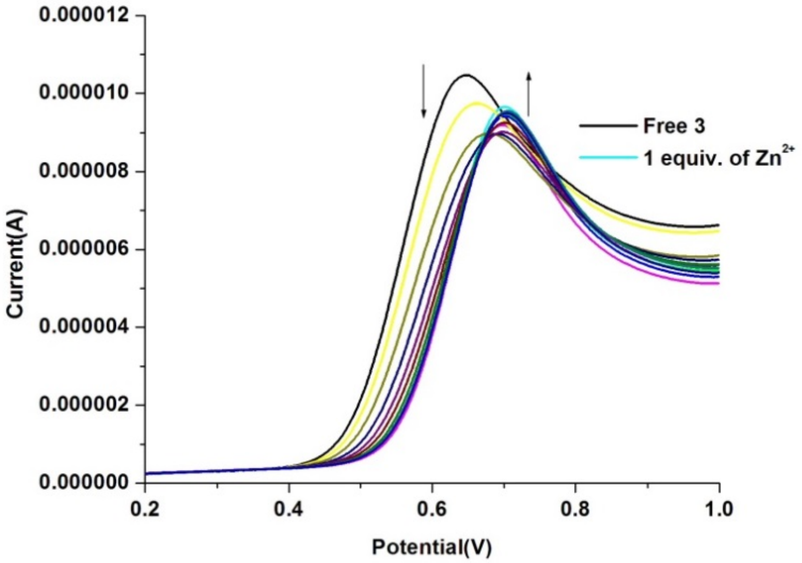

Fig. S35. Evolution of LSV of **3** ($1x10^{-4}$ M) upon addition of Zn^{2+} up to 1 equivalent with $[(n-Bu)_4N]ClO_4$ as supporting electrolyte. Scan rate employed 0.1 VS^{-1}

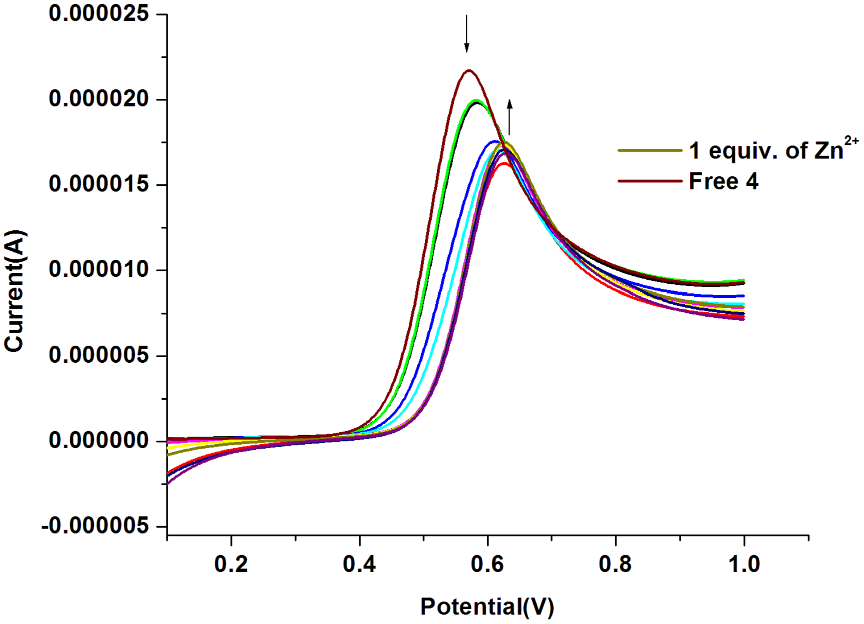

Fig. S36. Evolution of LSV of **4** ($1x10^{-4}$ M) upon addition of Zn^{2+} up to 1equivalent with $[(nBu)_4N]ClO_4$ as supporting electrolyte. Scan rate employed 0.1 VS^{-1}

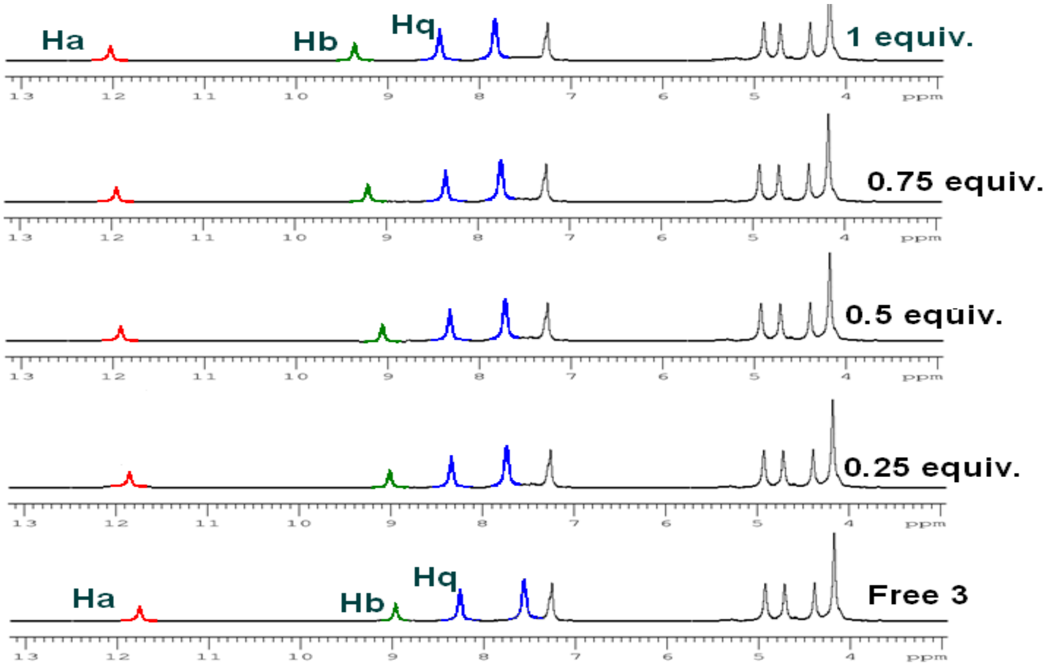

Fig. S37. ^{1}H NMR titration of **3** (10^{-5} M) upon addition of Zn^{2+} ions in DMSO-d_6.

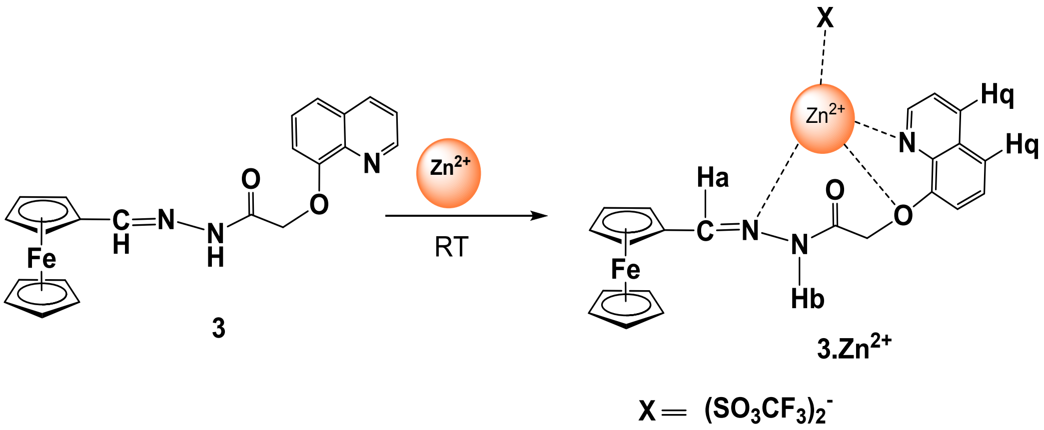

Scheme S2. Plausible binding mode for **3** with Zn^{2+}.

In order to understand the binding mechanism, ^{1}H NMR titration was performed by concomitant addition of Zn^{2+} to the DMSO-d_6 solution of **3**. As illustrated in (Fig. S37) significant shifts in ^{1}H NMR spectrum were observed upon addition of Zn^{2+}. After five minutes of addition of Zn^{2+} to **3**, the peaks related to imine protons Ha, Hb and quinoline ring protons Hq were shifted downfield by ca. 0.3, 0.45 and 0.18 ppm, respectively. Such downfield shifts of quinoline ring proton and

Ha, Hb in the metal complex of **3** indicated that Zn^{2+} was chelated by imine and quinoline ring nitrogen atoms as shown in scheme S2.

References:

1. M. Ahmed, R. Sharma, D. P. Nagda, G. A. Talesara and G. A. Arkivoc Xi 2006, 66.
2. Crys Alis Pro, Version 1.171.33.66; Oxford Diffraction Ltd.: Abingdon, U.K., 2010.
3. G. M. Sheldrick, SHELXS ‘97 and SHELXL ‘97. University of Göttingen, Germany, 1997.
4. A. L. Spek, PLATON, A Multipurpose Crystallographic Tool, Utrecht University, Utrecht, The Netherlands, 2005.
5. S. Bala, A. Goswami, S. Sengupta, S. Ganguly, S. Bhattacharya, S. Khanra, and R. Mondal, *Cryst. Growth Des.*, 2013, **13**, 5068.